

See discussions, stats, and author profiles for this publication at: <https://www.researchgate.net/publication/272295700>

Synthesis of CuBO₂ Nano/Microrods via Easy Molten Salt Route and Study of Its Field Emission Properties

ARTICLE in CRYSTAL GROWTH & DESIGN · FEBRUARY 2015

Impact Factor: 4.89 · DOI: 10.1021/cg5018906

READS

89

5 AUTHORS, INCLUDING:



Saswati Santra

Jadavpur University

11 PUBLICATIONS 26 CITATIONS

[SEE PROFILE](#)



Nirmalya Sankar Das

Jadavpur University

40 PUBLICATIONS 189 CITATIONS

[SEE PROFILE](#)



Diptonil Banerjee

Academy of Technology

41 PUBLICATIONS 241 CITATIONS

[SEE PROFILE](#)

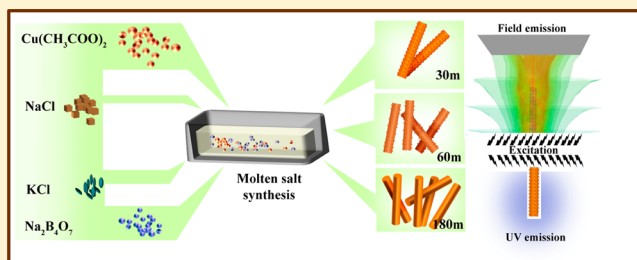
Synthesis of CuBO₂ Nano/Microrods via Easy Molten Salt Route and Study of Its Field Emission Properties

Saswati Santra,^{†,§} Nirmalya S. Das,^{†,§} Biswajit Das,[‡] Diptonil Banerjee,[‡] and Kalyan K. Chattopadhyay*,^{†,‡}

[†]Thin Film & Nanoscience Laboratory, Department of Physics, and [‡]School of Materials Science and Nanotechnology, Jadavpur University, Kolkata 700 032, India

Supporting Information

ABSTRACT: Nanostructures of copper based delafossites, which are p-type transparent conducting oxides (p-TCO), are technologically very important. Nanorods of CuBO₂, the latest member in the family of p-TCO, were prepared via easy molten salt method for the first time. The synthesis was optimized by varying the molarity of the precursor and synthesis parameters. The prepared samples were characterized by X-ray diffraction for structural information. Field emission scanning electron microscopy and transmission electron microscopy revealed the morphological nature of the samples. Compositional analyses were performed by energy dispersive analysis of X-rays. UV-vis-NIR spectrophotometric studies determined reflectance of the samples. Growth of CuBO₂ nanorods was correlated with synthesis duration. Photoluminescence properties of the sample were studied using a fluorometer. The electron field emission properties of the samples were measured using our laboratory-made high vacuum setup. Finite element based simulation studies were performed to explain and compare the field emission behavior with experimental outcome. It was observed that FE properties of the CuBO₂ nanorods were governed by both aspect ratio and the roughness of the nanorods.



INTRODUCTION

Oxide nanostructures have been widely studied during last few decades for exploring their application-worthy optical and electrical properties.^{1–5} Smart devices used in solar cells,^{6–8} electrochromic devices,⁹ gas sensors,¹⁰ and flat panel displays¹¹ often contain such multipurpose oxide nanostructures in various forms like nanocrystals,⁸ nanospikes,¹ nanopants,¹² thin films,³ etc. However, industrial usage of TCO nanostructures are mainly dominated by n-type oxides like SnO₂, ZnO, In₂O₃, etc.,^{11–14} and their p-type counterparts are comparatively less used for these purposes. The reason is p-type TCOs are generally considered to exhibit inferior electrical conductivity compared to the n-types, and thus they are not appropriate candidates to be used in smart applications like “invisible electronics”.¹⁵ Strongly localized nature of p orbitals in O 2p states in p-type binary oxides restricts carrier mobility for holes and therefore introduces a harder barrier for obtaining appreciable conductivity. Doping of n-type oxides sometimes solves the problem partially, but the necessity of development of highly conducting intrinsic p-type TCOs can never be ignored. The first successful attempt toward this was reported by Kawazoe and his co-workers¹⁶ who introduced the theory of “chemically modulated valence band” and smart p-type TCO CuAlO₂ having enhanced electrical conductivity and good transparency. Exploiting the principle of chemical modulation of valence band, several cooper based delafossites were developed having CuMO₂ structure with M as Cr, Fe, Ga, Sc, Y, etc.^{17–20} Those Cu delafossites and their nanostructures

exhibit very high conductivity and appreciable transmittance, fulfilling the criteria of a proper p-type semiconductor opening up new possibilities for fabrication of high figures of merit junction based devices and several other applications like photocatalysis,²¹ photodiodes,²² sensing,²³ etc. In some of our earlier studies, we reported high performance cold cathodes^{24,25} and thermoelectric²⁶ systems involving CuAlO₂. We also extended this work on the new copper delafossite CuBO₂ which was first reported by Snure et al. in 2007.²⁷ Again theoretical studies by Nie et al. indicated that copper delafossites having CuMO₂ form should exhibit larger optical band gap as the ionic radius of M decreases,²⁸ and Snure et al. showed that CuBO₂ has the largest band gap among the delfossite family.²⁷ We also showed that this novel ternary oxide has wonderful application oriented properties like photocatalysis,²⁹ junction based performance,³⁰ photoconductivity,³¹ luminescence,³² etc. Moreover, it was earlier reported that like all other semiconductor TCOs, copper delafossites also exhibit enhanced opto-electrical properties in lower dimension.^{29,33} Rigorous scientific research has been carried out to explore newer applications involving nanostructures of those materials. Several synthesis techniques like PLD,²⁷ spray technique,³⁵ sputtering,²⁴ hydrothermal,³⁰ and sol-gel^{34,37} were developed for production of nanostructures of Cu delafossites to achieve

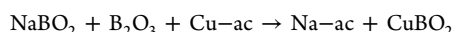
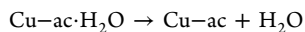
Received: December 30, 2014

Revised: January 30, 2015

industry friendly production route. All of the traditional methods have their own merits and drawbacks. Physical routes like sputtering or PLD require complicated synthesis setup which is not financially suitable. Chemical techniques like sol-gel technique offer less tunability of dimension of nanostructures which is inevitable for better control over the properties of those nanostructures. Open air solid-solid reaction has also been widely employed to synthesize CuAlO_2 using oxides of the precursor materials.^{16,38} But the same is not facile for synthesis of CuMO_2 where M is a light element like B. From this point of view, molten salt synthesis is an easy and effective method which has been employed to obtain Cu delfosse nanostructures (having a light element) with desirable dimension and excellent opto-electrical properties of the same. In addition to that, molten salt synthesis technique is considered to be an effective route to synthesize large amount of target material in a comparatively short synthesis time.^{39–41} After preparation of novel CuBO_2 via sol-gel, hydrothermal technique, in this work, we have employed this novel production route to synthesize CuBO_2 nanostructures. Inspired by excellent field emission behavior of CuAlO_2 and also for CuBO_2 nanoparticles reported in our earlier works,⁴² we have studied the field emission behavior of CuBO_2 micro/nanorods for the first time. Moreover, some important optical and physical properties like reflectance and photoresponse of this novel nanostructured material were also investigated for the first time. The cold electron emission properties of the samples were simulated using finite elemental analysis by ANSYS software. All the results were correlated, and it was observed that the FE behavior of the as synthesized CuBO_2 nanorods was dependent not only on the aspect ratio of the nanostructure but also on the roughness and defects of the same.

EXPERIMENTAL SECTION

Commercially available copper acetate, borax, sodium chloride, and potassium chloride were used as starting materials. For the optimization of the synthesis of proper phase CuBO_2 , various synthesis parameters were varied. For example, those precursors were mixed with various stoichiometric ratios (1:0.25:20:20, 1:0.25:30:30, 1:0.25:40:40). These materials were then taken in a mortar pester and grinded manually for 30 min to mix them properly. The ground powder mixtures were taken into alumina boats and annealed in furnace at various temperatures (800, 850, and 900 °C) and for different time intervals of 30, 60, 180, 300, and 600 min. All the samples were cooled naturally at room temperature. The obtained deep brown products were thereafter washed in deionized water and filtered several times to remove the residual salts. The residue was dried in an oven at 60 °C for 24 h. The dried powder was then collected for further characterization. Additionally the probable chemical reaction involved behind the production of CuBO_2 may be written as the following:



CHARACTERIZATION

The as prepared samples were characterized by X-ray diffractometer (XRD; Bruker, D-8 Advance) with the Cu K_α radiation of wavelength $\lambda = 1.5406 \text{ \AA}$ for crystalline phase information. Figure 1a shows the XRD patterns of samples prepared at 800, 850, and 900 °C where it can be seen that the

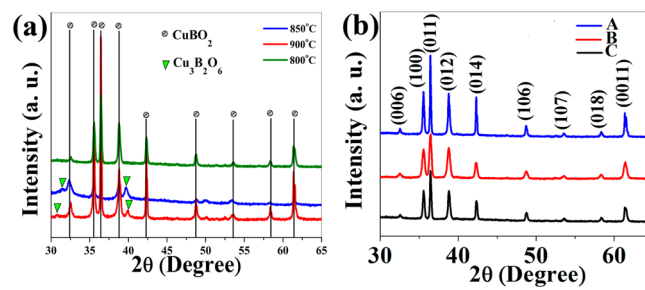


Figure 1. (a) XRD pattern of samples annealed at different temperatures; (b) XRD pattern of samples prepared at different durations.

samples prepared at 850 and 900 °C contain the presence of some $\text{Cu}_3\text{B}_2\text{O}_6$ in addition to standards of the desired crystalline phase of CuBO_2 . Hence the optimized synthesis temperature was taken at 800 °C. The other synthesis parameters like molarity of precursors and synthesis duration were also optimized for achieving the desired crystalline phase and sample morphology. Finally the samples having proper phase and good nanostructure were considered for further characterization. The details of the sample characterizations for optimization process are provided in the Supporting Information. It was found that the samples prepared in 1:0.25:40:40 stoichiometric ratio and annealed at 800 °C for 30, 60, and 180 min (labeled as sample A, B, and C, respectively) exhibit proper crystalline phase, and hence further characterizations were carried out with those samples only. The morphological properties of the as prepared samples were characterized by a field emission scanning electron microscope (FESEM, Hitachi, S-4800). Transmission electron microscopic (JEOL, 200 kV HRTEM) imaging revealed the exact dimensions and lattice spacing along with selected area electron diffraction (SAED) pattern. Compositional analysis of the as prepared samples was performed using energy dispersive X-ray tool attached with scanning electron microscope. The optical properties and various optical parameters of the CuBO_2 samples were studied by UV-vis spectrophotometer (Shimadzu UV-3600). Luminescence properties of samples A, B, and C were studied by fluorometer (Elico, India). Photoresponse properties of the as prepared samples in pellet form were investigated using standard $I-V$ measurement setup. For this, silver metallic contacts were deposited on the pellets at a distance of 1 cm. Visible light from a tungsten lamp (Philips) with a measured light intensity of 9.45 mW cm^{-2} was used as the source of excitation.

Field emission properties of the as prepared nanostructures were studied using our laboratory made high vacuum field emission setup. Finite element electrostatic simulations using "ANSYS Maxwell" software were carried out to investigate the effects of shape and morphology and the screening effect of the as prepared nanostructures, and the results were compared with experimental outcome.

RESULTS AND DISCUSSION

Structural and Compositional Studies. Figure 1b represents the XRD patterns of the samples. Intense diffraction peaks can be found indicating good crystallinity of the samples. The peaks near 32° , 35° , 36° , 38° , 42° , 48° , 53° , 58° , and 61° were assigned to be arising due to reflection from (006), (100), (011), (012), (014), (106), (107), (018), (0011) planes respectively of CuBO_2 lattice (JCPDS 28-1256). The d spacings

were calculated using standard Bragg's equation and lattice parameter values²⁷ $a = b = 2.84 \text{ \AA}$ and $c = 16.52 \text{ \AA}$. The results are presented in Table 1 which is correlated with micrographic observation (discussed later).

Table 1. d spacing for Various Crystalline Planes of the CuBO₂ Samples

planes (<i>hkl</i>)	d spacing (Å)		
	sample A	sample B	sample C
(006)	2.75069	2.7512	2.74951
(100)	2.52434	2.52402	2.52273
(011)	2.46479	2.46489	2.46344
(012)	2.32023	2.32085	2.35991
(014)	2.13463	2.13544	2.13336
(106)	1.86809	1.86812	1.8671
(107)	1.71021	1.71092	1.70969
(018)	1.5807	1.58155	1.58034
(0011)	1.5085	1.50892	1.50812

The EDX analysis of sample revealed that all the constituent elements, i.e., copper, boron, and oxygen, were present within the sample, and the results are depicted in Figure 2. The atomic

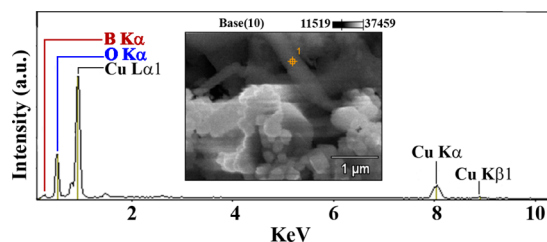


Figure 2. EDX spectra of the sample (inset shows the point of measurement).

ratio of B:Cu:O was found to be 1:1.35:1.70. The comparatively lesser amount of boron can be accounted for by its low atomic weight which may affect the atomic percentage of boron during electron bombardment of EDX measurement procedure. However, the sample was found to exhibit oxygen deficiency. The observed oxygen deficiency was also revealed in luminescence studies, and the same was correlated with synthesis parameters as discussed later in the Luminescence Studies section.

Morphological Studies. Figure 3 depicts the FESEM images of the as prepared samples. We can see that the number of microrods gradually increases from sample A to C as the synthesis duration increases (Figure 3a, c, e). The higher magnification images also describes that the roughness of individual microrods decreases as the synthesis duration increases. The growth mechanism of the rods can be illustrated using the micrographs. As we can see in Figure 3b, several particulated structures are attached to the main rod resulting in considerable roughness of the same. These irregularly shaped particles gradually decrease in number as the synthesis time increases, which is clearly observed in Figure 3d and f. Sample C exhibits smoothest surface with a very few number of irregular attachments, and the most important observation is presented in Figure 3f where it can be seen that the nanostructures are actually formed by thinner nanorods which were bundled to form the CuBO₂ microrods.

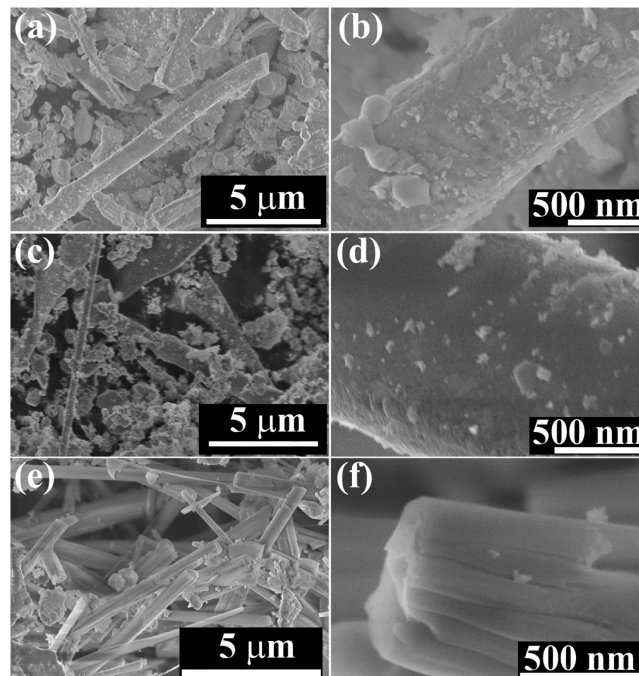


Figure 3. FESEM images of sample A (a) and (b); sample B (c) and (d); sample C (e) and (f).

Transmission electron micrographic studies were carried out for sample C to know the exact dimension and crystallographic information of the bundled nanorods. The results are presented in Figure 4a–d. Figure 4a depicts some bundled microrods, whereas it can be found from Figure 4b that the tips of the individual nanorods have less than 100 nm diameter. The d spacing was measured to be 2.33 Å from Figure 4c which is in full agreement with our XRD results (Table 1). Distinct single crystalline nature of the rods can be concluded from Figure 4d

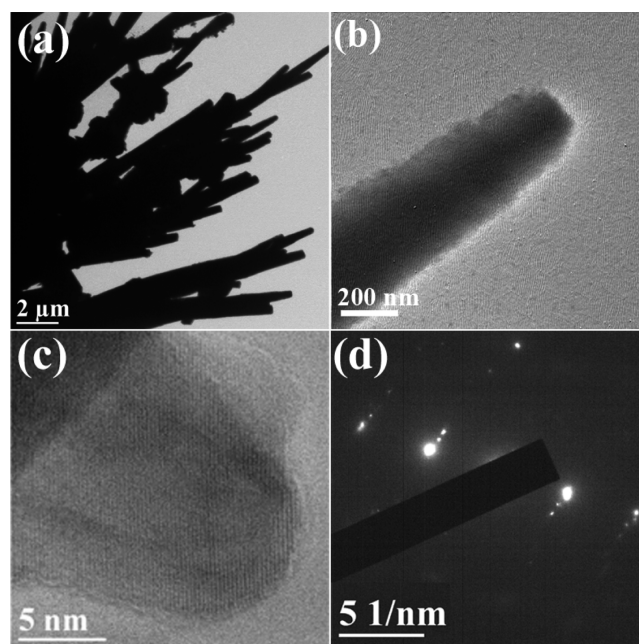


Figure 4. TEM image of nanobundles of sample C (a) and (b) single nanorod; (c) lattice image of one nanorod; (d) corresponding SAED pattern.

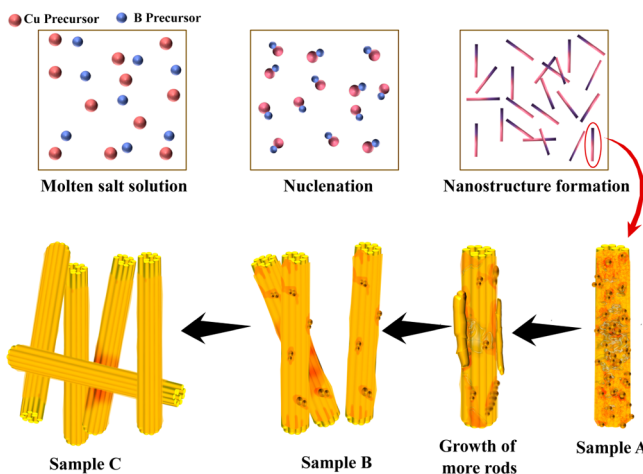
where the liner SAED spots were identified to be occurring due to diffraction from the (012) plane.

These observations from SEM and HRTEM micrograph can be used to explain the growth mechanism as the following.

Probable Growth Mechanism. Growth of the CuBO₂ rods can be explained in two phases; first, it is important to understand the growth of rodlike structure via molten salt process. Ternary oxide nanorods structures fabricated via molten salt process are often considered to be grown via some consecutive steps.⁴³ At primary stage, copper acetate used as precursor decomposed into its principal oxide, i.e., Cu₂O. Cu₂O and borax then dissolve into the molten salt. After the two oxides properly dissolved into molten salts, homogeneous nucleation process takes place. Then they yield compound oxide nanocrystals. Furthermore, within those nanocrystal products, growth of 1D nanorods starts in a specific crystallographic orientation, i.e., along (012) plane, along which the growth rate is higher than the other planes. This anisotropic crystal growth finally resulted in single crystal CuBO₂ nanorods.

However, it is also important to explain the presence of irregularly shaped nanoparticles which disappeared gradually as the synthesis time increased and is reflected in magnified SEM images (Figure 3b, d, f). As we discussed above, CuBO₂ nanorods start growing from compound CuBO₂ nanocrystals. In sample A, we find several such irregular attachments on the CuBO₂ nanorod-bundle surfaces. Those are nothing but the primary CuBO₂ nanocrystals which could not grow further to form CuBO₂ nanorods due to shorter synthesis duration. When further growth time was allowed in the case of sample B, they also grew into CuBO₂ nanorods and detached from the previous host bundle surface leaving less roughness of the same (Figure 3d). Still there were some CuBO₂ nanocrystals left which gradually turned into more nanorods as the synthesis time was further increased in the case of sample C. The newly formed CuBO₂ nanorods combined into newer bundles and separated from the previous host bundle to minimize surface energy. Thus, the bundles become comparatively smooth as almost the entire amount of precursors was converted into nanorods (and bundles). Scheme 1 presents the possible growth steps of the CuBO₂ bundles showing the gradual growth and separation of nanorods bundles as discussed above.

Scheme 1. Probable Growth Mechanism of CuBO₂ Nanorods and Nanobundles



It is also to be mentioned that the morphology of the samples prepared with higher synthesis duration (although exhibiting trace amount of impure phase) were also in full accordance to the above-mentioned mechanism and strongly support the same (please see Supporting Information).

Optical Studies. Reflectance Studies. The reflectance properties of the as prepared samples were measured using standard reference BaSO₄ compound. The obtained results are depicted in Figure 5. All the samples showed moderate

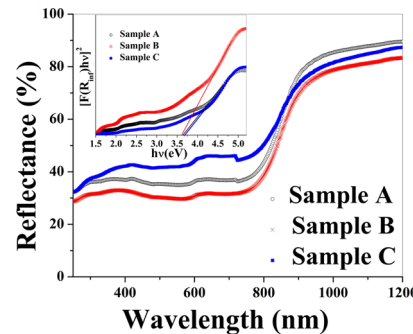


Figure 5. (a) Reflectance spectra (inset) band gap of sample A, B, and C.

reflectance of light within the visible region. The modified Kubelka–Munk (K–M) theory⁴⁴ was used to determine the optical band gaps of the as prepared samples using diffuse reflectance spectrum. For this, the common method is to measure the ratio of the light scattered by a thick layer of sample and a perfectly nonabsorbing reference sample as a function of the incident wavelength (λ). This may be written as following⁴⁴

$$R_{\infty} = R_{\text{sample}}/R_{\text{reference}}$$

Now the modified K–M function $F(R_{\infty})$ is related to relation between scattering coefficient S , diffuse reflectance of the sample R_{∞} , and the absorption coefficient K by the following equation

$$F(R_{\infty}) = \frac{(1 - R_{\infty})^2}{2R_{\infty}} = \frac{K}{S} \quad (1)$$

Again, the optical energy gap E_g of any sample satisfies a simple relation with linear absorption coefficient α as

$$\alpha h\nu = A(h\nu - E_g)^{1/2} \quad (2)$$

Here, A is a proportionality constant and ν is the incident photon energy. The absorption coefficient K is equal to the value of 2α if the material under test scatters diffuse light perfectly. If we consider the scattering coefficient does not vary with incident wavelength, the above eqs 1 and 2 give us the following expression for K–M function $F(R_{\infty})$

$$[F(R_{\infty})h\nu]^2 = B(h\nu - E_g) \quad (3)$$

Now if $[F(R_{\infty})h\nu]^2$ is plotted as a function of $h\nu$, the extrapolation of the linear part of the plot should give the optical energy gap, i.e., E_g . In our observed result following the above calculation two regions, one linear and another nonlinear portion were observed as expected in any direct allowed transition (Figure 5). The residual absorption corresponding to

impurity states contributes to the linear part, and the fundamental absorption may be accounted for the liner portion.

Employing the above procedure, the optical band gaps observed for the as synthesized samples are clearly depicted in the inset of Figure 5. It is observed that all the CuBO₂ nanostructures exhibit wide optical band gap ranging from 3.66 to 3.69 eV. The results are in good agreement with previous reports regarding this novel delafossite.³⁶ The variation of band gap, although very small in value, cannot be correlated to the dimensions of the nanostructures, i.e., quantum confinement effect, etc., as the samples contain mixed geometrical shape (nanoparticles and nano/microrods) depending upon the reaction time. However, all the samples exhibited wide band gaps in the UV-range.

Luminescence Studies. Photoluminescence emission spectra of the as prepared samples were recorded via exciting the samples by 236 nm UV light, and the observed results are presented in Figure 6a–d. All of the samples showed broad

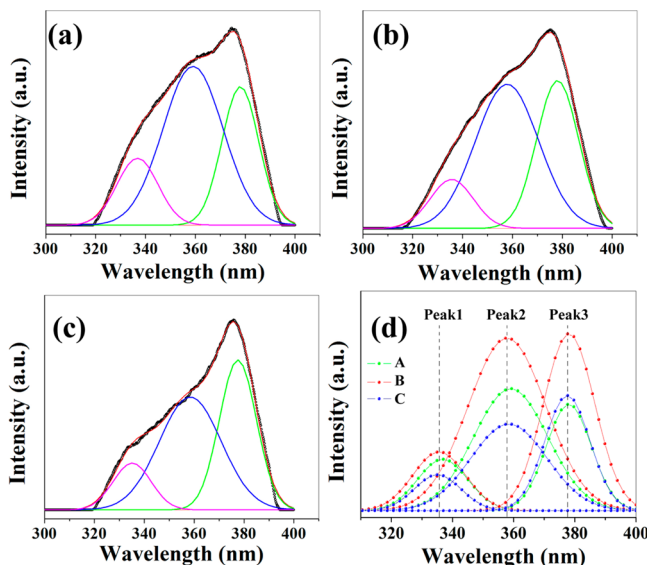


Figure 6. Deconvoluted photoluminescence spectra of (a) sample A; (b) sample B; (c) sample C, and (d) relative positions of deconvoluted peaks.

emission peaks in the UV range. The emission peaks were further deconvoluted to find out different interlaying peaks arising due to band to band and defect related transitions. Until now CuBO₂ nanostructures were reported to exhibit wide band gaps around 3.6 eV.^{30,34} Before assigning the first peak arising near 335 nm to band to band transition, we must keep in mind that generally at low temperature, wide band gap oxide semiconductors mainly show bound excitonic emission properties. But at room or higher temperatures, strong localization of electron–hole pairs gives rise to free excitonic emission. However, recently, Wu et al.⁴⁵ reported that undoped wide band gap semiconductors exhibiting good crystallinity can show room temperature UV emission occurring due to free excitonic recombination near band edge, as also mentioned by Banerjee et al.⁴⁶ We can therefore attribute the first peak arising near 335 nm to band to band transition. However, deconvolution of room temperature PL spectra of all the samples show two other peaks also. Mo et al.⁴⁷ also observed similar kinds of PL peaks for CuAlO₂ nanowires near 350 nm and attributed the same to the electron configuration transition in Cu⁺ ions under

excitation, i.e., 3d⁹4s¹–3d¹⁰. However, according to us, the peaks arising near 357 and 377 nm can be correlated to oxygen vacancies and defects present in our CuBO₂ nanostructure samples. A supporting logic behind this speculation may be that, first of all, we should remember that we have prepared our samples just varying time; precursor concentrations and other parameters were kept the same for all three samples. It is expected that the atomic defects do not change in nature much if those parameters are kept the same; only the nanostructure dimensions change, and the defect density may be varied due to increased synthesis duration. Also, it is reported that PL peaks show considerable red/blue shift with change of defect states.^{48,49} Peak shift is also observed in the case of change of nanoparticle diameter⁵⁰ of the experimental samples. In our case, no appreciable shift is observed for any of the peaks for any samples (Figure 6a–c). Morphological studies confirmed that the CuBO₂ samples cannot be treated as nanoparticles either. So it may be inferred that the other two peaks observed in luminescence spectra may be contributed from defect states which remained almost in the same position indicating no change of nature of such defects. However, the defect densities changed, which is revealed in Figure 6d. This variation of defect densities were also reflected in the field emission properties of the as prepared samples (discussed later).

Photoresponse Studies. For measuring photoresponse property, all the samples were pelletized by applying 20 kN hydrostatic pressure. The pellets (1.5 cm diameter and 0.1 cm width) were then used for *I*–*V* measurement in the dark and under illumination of visible light. The experimental setup for the measurement has been schematically represented in Figure 7a. It can be clearly seen that all the samples showed good

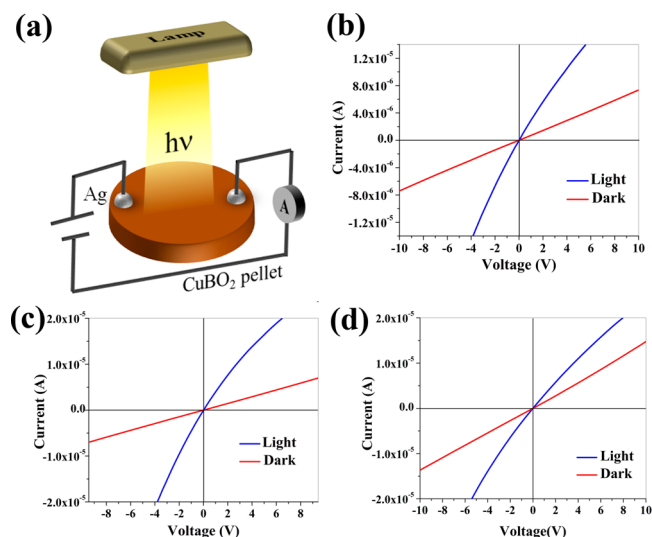


Figure 7. (a) Schematic diagram of the circuit connection to study photoresponse of CuBO₂ samples; (b), (c), (d) photoresponse characteristics of the samples A, B, and C, respectively.

photoresponse with an appreciable increment of current after exposure of visible light. The values of $I_{\text{ph}}/I_{\text{dark}}$ were determined for a particular voltage; they were within the range 2.08–4.53. The excitation introduced by the visible light photon may be accounted for by the observed photoresponse property.

Field Emission Studies. Field emission properties of samples A, B, and C were carried out in our homemade high vacuum field emission setup by using a diode configuration consisting of

a cathode (which is made of the sample under test) and a stainless steel tip anode of conical shape having a tip diameter of 1 mm. The measurements were carried out after evacuating the chamber up to $\sim 10^{-7}$ mbar base pressure. The interelectrode separation was made adjustable to a few hundred micrometers by means of a micrometer screw, and the measurements were performed keeping tip–sample distance at 150 μm . The surface of the sample was kept under observation through the chamber view port, which enabled us to recognize any discharge, if occurring at all. It was confirmed that no discharge occurred during the application of high electric field, and hence the currents observed in these measurements were considered to be cold field emission of electron from the samples.

Theoretically, the emission current I is related to the macroscopic electric field E by

$$I = Aa\phi^{-1}(\beta E)^2 \exp[-b\phi^{3/2}(\beta E)^{-1}] \quad (4)$$

where ϕ and β are the local work function and the field enhancement factor respectively, A is the effective emission area, a , b are Fowler–Nordheim constants having values $a = 1.56 \times 10^{-10} \text{ A eV V}^{-2}$ and $b = 6.83 \times 10^3 \text{ eV}^{-3/2} \text{ V } \mu\text{m}^{-1}$. The applied macroscopic field E was determined by dividing the external voltage (V) by the actual interelectrode distance d which was maintained the same (150 μm) throughout the experiment.

Equation 4 may be rewritten in the following form

$$\ln\left(\frac{J}{E^2}\right) = \ln(a\phi^{-1}\beta^2) - \frac{b\phi^{3/2}\beta^{-1}}{E} \quad (5)$$

So a plot of $\ln\{J/E^2\}$ vs $1/E$ should be geometrically a straight line. Important information about the field enhancement factor (β) and local work function (Φ_{eff}), etc., can be derived from its slope (m) and intercept. For this, the following relations were used

$$\beta = -b\Phi^{3/2}/m \quad (6)$$

and

$$\Phi_{\text{eff}} = \Phi/\beta^{2/3} \quad (7)$$

Experimentally observed current voltage data was further plotted to obtain J – E curves which are presented in Figure 8a. We can see that the samples show appreciably high current density up to the mA/cm^2 range. The turn-on field was defined as the field required for achieving an emission current density of 0.3 $\mu\text{A/cm}^2$, and considering that, the turn-on fields were determined from the J – E curves. Figure 8b depicts the variation of turn-on field with synthesis duration where we

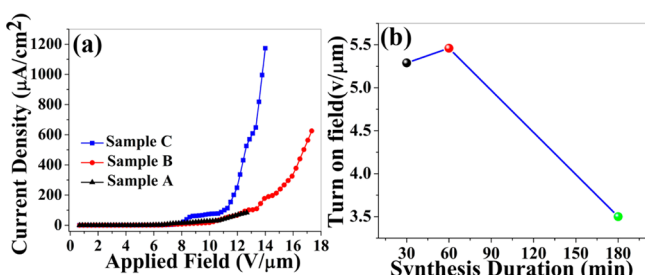


Figure 8. (a) Field emission J – E curves of the samples; (b) turn-on voltages of the samples.

can see that sample C showed the lowest turn-on field which is higher for sample B and C. The F–N plots obtained from the J – E curves are presented in Figure 9a, where we can see all the

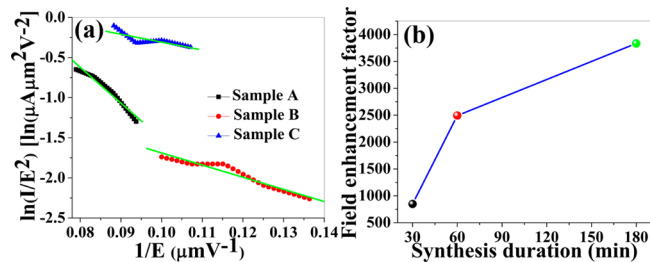


Figure 9. (a) F–N plots derived from field emission curves for the samples; (b) field enhancement factors for the samples.

samples showed linear nature and negative slopes confirming the cold cathode emission behavior of the samples. The field enhancement factors calculated using eq 6 are presented in Figure 9 b. We can see that field enhancement factors also increased for sample C and gradually decreased for sample A.

Now, for explaining the field emission properties of the as prepared CuBO₂ nanobundle samples, we must take into account two factors affecting the same: first, the nanostructural properties and second, the effect of defects present within the samples.

If we carefully observe the FESEM images, we may find that the nanobundles in sample A are not fully grown and many irregularly shaped nanoparticles are present there. Moreover, the nanobundles are rarest in number in sample A whereas sample C contains mostly pure nanobundles and the least number of randomly sized nanoparticles. According to our best understanding, CuBO₂ nanobundles are the main emitters. Nanoparticles are rather inferior emitters due to lesser aspect ratio compared to the nanobundles. As a result sample C showed very high emission current density with (Figure 8a) lowest turn-on field and highest field enhancement factor. Similarly, the mentioned emission parameters gradually became inferior in the case of samples B and A. However, if we carefully look at Figure 8a, it may be noticed that at low field, there are some sections where sample A shows slightly higher current density than sample B. Geometry of the nanostructures cannot solely explain the above anomaly. It is of interest to consider the effect of defect states present in the prepared samples on this nature of emission behavior at low field. For this, we have taken into account the relative intensity of the PL peaks arising due to defect states. These defect states often act like local adsorption sites and chemisorb atmospheric O₂ molecules to form O₂⁻ at room temperature.⁵¹ Surface electrons are deflected by this generated O₂⁻ which adds additional barrier potential. We can see in Figure 10 that the relative intensity of defect related peaks is higher in the case of sample B than those for sample A. We had similar observations in our earlier work where defects present in ZnO nanoparticle coated over well-known emitter Si nanowire governed the FE properties.⁵² Hence sample B having higher defect density than sample A resulted in comparatively inferior emission density at low field region.

Again, we can see that sample C has lesser defect density than sample B but comparatively higher than that of sample A. But the emission current density is always higher for sample C than sample B and C. This may be correlated with intrinsic

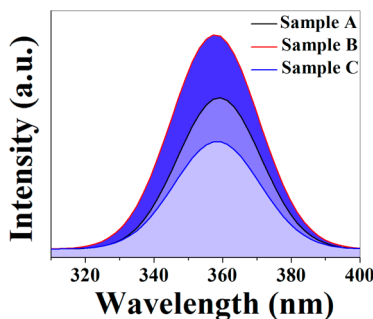


Figure 10. Relative intensities of the defect related luminescence peaks for all the samples.

conductivity of the samples. From Figure 5, we can see that the sheet resistance is much lower in the case of sample C whereas sample A and B exhibit almost the same values of sheet resistance. Due to this career-rich nature, sample C is not much affected by defect density and showed better emission current density consistently in both low and high field region. However, samples B and A have resistance very close to each other, so sample B having higher defect density sometimes showed lesser emission current. But at high field region, external applied field is sufficiently high to overcome the barrier caused by generated O_2^- and results in higher current density than that of sample A. It is to be mentioned here that the emission current density obtained from the most efficient emitter sample is much higher than that of the finest CuBO₂ nanoparticle emitters as reported in our previous work.⁴²

Simulation of FE Properties Using ANSYS. The variation of field emission current density was further simulated employing finite element analysis by ANSYS software. In this simulation method, electrostatic analysis is carried out surrounding the model nanostructures (CuBO₂ nanostructures, in our case) to determine the electric field distribution. Basically Poisson's equation in electrostatic as given by eq 8 is solved with appropriate boundary conditions

$$\nabla^2 V = 0 \quad (8)$$

The boundary conditions were established by setting the sample at ground potential and the anode electrode at applied bias potential. The space charge effects and variation of electric field due to emitted electrons were not taken into account in the calculations as they have negligible effect.⁵³

In detail, a 2D model of CuBO₂ nanostructures was considered keeping the dimensions as exactly observed in morphological studies. The interelectrode separations were kept at 150 μm as per actual basis. Both single nanobundle and array of nanobundles were modeled to theoretically observe the distribution of emitted electric field. The results of simulation studies are presented in Figure 11a–f. In Figure 11a, single emitter similar to sample A showed the least amount of emitted field which gradually increased for model of sample B (Figure 11c) and sample C (Figure 11e).

The assembly of such single emitters of sample A, B, and C was also considered which is closer to actual experimental case. The output of simulation clearly showed that sample C is expected to emit higher density of emission current (Figure 11b) than sample B (Figure 11d) or sample A (Figure 11f) covering larger area of high field region. These simulation results are in full agreement with our experimental observation.

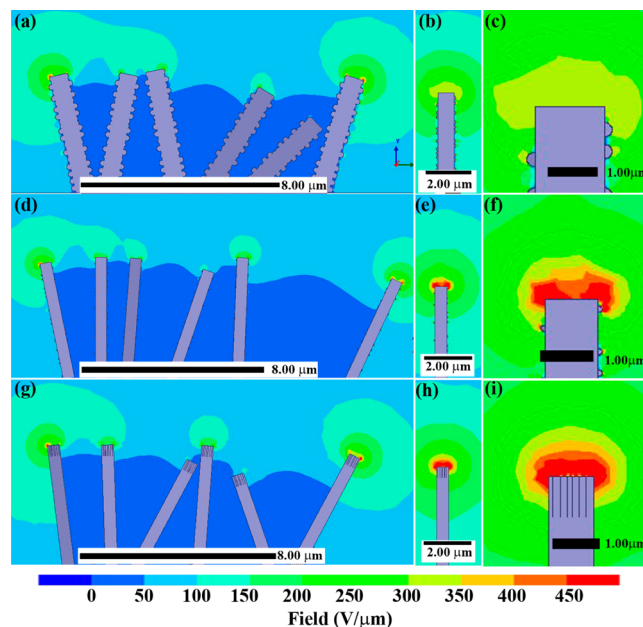


Figure 11. Computed results of electric field for (a) single emitter, (b) array of emitters of sample A; (c) single emitter, (d) array of emitters of sample B; (e) single emitter, (f) array of emitters of sample C.

CONCLUSION

CuBO₂ nanobundles were synthesized for the first time via easy molten salt method by varying the synthesis duration. The XRD studies confirmed proper phase formation. Morphological studies were carried out using FESEM and HRTEM which showed nanorods and nanobundle-like structure of the as prepared samples and also revealed the single crystalline nature of the same. The growth mechanism of the nanostructures was discussed in detail. Reflectance studies were carried out to find out the band gap of CuBO₂ nanostructures, and the luminescence studies were also carried out. Field emission properties of the as prepared samples were studied in detail, and the same was supported by theoretical simulation performed using ANSYS. It was observed that the emission behavior is controlled by both defect states and morphology of the nanostructures. It was also confirmed that simply varying the synthesis duration control over the turn-on field and emission current density can be achieved, which are the key factors of emission display fabrication.

ASSOCIATED CONTENT

Supporting Information

XRD pattern and FESEM images of the samples prepared using precursor molar ratios of 1:0.25:20:20 and 1:0.25:30:30; XRD pattern and FESEM images of the samples prepared with synthesis duration of 300 and 600 min; a brief discussion on the applicability of the proposed growth mechanism for the samples prepared in even nonoptimized conditions. This material is available free of charge via the Internet at <http://pubs.acs.org/>.

AUTHOR INFORMATION

Corresponding Author

*Fax: +91 33 2414 6007. E-mail address: kalyan_chattopadhyay@yahoo.com.

Author Contributions

[§]S.S. and N.S.D. contributed equally to this work and should be considered cofirst authors.

Notes

The authors declare no competing financial interest.

ACKNOWLEDGMENTS

One of us (S.S.) thanks the Dept. of Science and Technology, the Govt. of India for providing her “Inspire Fellowship”. The authors also thank the DST for a project support and the University Grants Commission, the Govt. of India (UGC), for “University with potential for excellence (UPE II)” scheme.

REFERENCES

- (1) Jebril, S.; Kuhlmann, H.; Muller, S.; Ronning, C.; Kienle, L.; Doppel, V.; Mishra, Y. K.; Adelung, R. *Cryst. Growth Des.* **2010**, *10*, 2842–2846.
- (2) Yoon, S. W.; Seo, J. H.; Seong, T. Y.; Yu, T. H.; You, Y. H.; Lee, K. B.; Kwon, H.; Ahn, J. P. *Cryst. Growth Des.* **2012**, *12*, 1167–1172.
- (3) Lee, J. H.; Ko, K. H.; Park, B. O. *J. Cryst. Growth* **2003**, *247*, 119–125.
- (4) Sato, H.; Minami, T.; Takata, S.; Yamada, T. *Thin Solid Films* **1993**, *236*, 27–31.
- (5) Soylu, M.; Al-Ghamdi, A. A.; Omran, S. B.; Yakuphanoglu, F. *J. Alloys Compd.* **2014**, *617*, 602–608.
- (6) Stannowski, B.; Ruske, F.; Neubert, S.; Schönau, S.; Ring, S.; Calnan, S.; Wimmer, M.; Gabriel, O.; Szyszka, B.; Rech, B.; Schlatmann, R. *Thin Solid Films* **2014**, *555*, 138–142.
- (7) Zhang, R.; Kumar, S.; Zou, S.; Kerr, L. L. *Cryst. Growth Des.* **2008**, *8*, 381–383.
- (8) Wu, J.; Hao, S.; Lin, J.; Huang, M.; Huang, Y.; Lan, Z.; Li, P. *Cryst. Growth Des.* **2008**, *8*, 247–252.
- (9) Granqvist, C. G.; Pehlivan, I. B.; Ji, Y. X.; Li, S. Y.; Niklasson, G. A. *Thin Solid Films* **2014**, *559*, 2–8.
- (10) Kevin, M.; Tho, W. H.; Ho, G. W. *J. Mater. Chem.* **2012**, *22*, 16442–16447.
- (11) Yang, B.; Kumar, A.; Zhang, H.; Feng, P.; Katiyar, R. S.; Wang, Z. *J. Phys. D: Appl. Phys.* **2009**, *42*, 045415/1–5.
- (12) Tiwari, A.; Snure, M. *J. Nanosci. Nanotechnol.* **2008**, *8*, 3981–3987.
- (13) Mazumder, N.; Sen, D.; Saha, S.; Ghorai, U. K.; Das, N. S.; Chattopadhyay, K. K. *J. Phys. Chem. C* **2013**, *117*, 6454–6461.
- (14) Jeong, J. A.; Jeon, Y. J.; Kim, S. S.; Kim, B. K.; Chung, K. B. *Sol. Energy Mater. Sol. Cells* **2014**, *122*, 241–250.
- (15) Thomas, G. *Nature* **1997**, *389*, 907–908.
- (16) Kawazoe, H.; Yasukawa, M.; Hyodo, H.; Kurita, M.; Yanagi, H.; Hosono, H. *Nature* **1997**, *389*, 939–482.
- (17) Varadarajan, V.; Norton, D. P. *Appl. Phys. A: Mater. Sci. Process.* **2006**, *85*, 117–120.
- (18) Park, S.; Kesler, D. A. *J. Solid State Chem.* **2003**, *173*, 355–358.
- (19) Moharam, M. M.; Rashad, M. M.; Elsayed, E. M.; Shahba, R. M. *A. J. Mater. Sci.* **2014**, *25*, 1798–1803.
- (20) Trari, M.; Bouguelia, A.; Bessekhouad, Y. *Sol. Energy Mater. Sol. C* **2006**, *90*, 190–202.
- (21) Keriche, N.; Bouguelia, A.; Aider, A.; Trari, M. *Int. J. Hydrogen Energy* **2005**, *30*, 693–699.
- (22) Gupta, R. K.; Cavas, M.; Al-Ghamdi, Ahmed A.; Gafer, Z. H.; El-Tantawy, F.; Yakuphanoglu, F. *Sol. Energy* **2013**, *92*, 1–6.
- (23) Zhou, S.; Fang, X.; Deng, Z.; Li, D.; Dong, W.; Tao, R.; Meng, G.; Wang, T. *Sens. Actuators, B* **2009**, *143*, 119–123.
- (24) Banerjee, A. N.; Ghosh, C. K.; Das, S.; Chattopadhyay, K. K. *Physica B* **2005**, *370*, 264–276.
- (25) Banerjee, A. N.; Chattopadhyay, K. K. *Appl. Surf. Sci.* **2004**, *225*, 243–249.
- (26) Banerjee, A. N.; Maity, R.; Ghosh, P. K.; Chattopadhyay, K. K. *Thin Solid Films* **2005**, *474*, 261–266.
- (27) Snure, M.; Tiwari, A. *Appl. Phys. Lett.* **2007**, *91*, 092123.
- (28) Nie, X.; Wei, S. H.; Zhang, S. B. *Phys. Rev. Lett.* **2002**, *88*, 066405–1.
- (29) Santra, S.; Das, N. S.; Chattopadhyay, K. K. *Mater. Res. Bull.* **2013**, *48*, 2669–2677.
- (30) Santra, S.; Das, N. S.; Maiti, S.; Chattopadhyay, K. K. *Chem. Phys. Lett.* **2014**, *604*, 97–100.
- (31) Santra, S.; Das, N. S.; Chattopadhyay, K. K. *AIP Conf. Proc.* **2013**, *1536*, 723–724.
- (32) Santra, S.; Das, N. S.; Chattopadhyay, K. K. *Proc. SPIE* **2012**, *8549*, 85491W–1–6.
- (33) Ruttanapun, C. *J. Appl. Phys.* **2013**, *114*, 113108/1–5.
- (34) Banerjee, A. N.; Joo, S. W. *Nanotechnology* **2011**, *22*, 365705/1–8.
- (35) Bouzidi, C.; Bouzouita, H.; Timoumi, A.; Rezig, B. *Mater. Sci. Eng., B* **2005**, *118*, 259–263.
- (36) Santra, S.; Das, N. S.; Chattopadhyay, K. K. *Mater. Lett.* **2013**, *92*, 198–201.
- (37) Ghosh, C. K.; Popuri, S. R.; Mahesh, T. U.; Chattopadhyay, K. K. *Sol.–Gel Sci. Technol.* **2009**, *52*, 75–81.
- (38) Mazumder, N.; Sen, D.; Ghorai, U. K.; Roy, R.; Saha, S.; Das, N. S.; Chattopadhyay, K. K. *J. Phys. Chem. Lett.* **2013**, *4*, 3539–3543.
- (39) Sen, A.; Maiti, U. N.; Maiti, S.; Chattopadhyay, K. K. *J. Mater. Sci.* **2013**, *48*, 3967–3974.
- (40) Yuvaraj, S.; Nithya, V. D.; Fathima, K. S.; Sanjeeviraja, C.; Selvan, G. K.; Arumugam, S.; Selvan, R. K. *Mater. Res. Bull.* **2013**, *48*, 1110–1116.
- (41) Kikuchihiara, A.; Sakurai, F.; Kimura, T. *J. Am. Ceram. Soc.* **2012**, *95*, 1556–1562.
- (42) Santra, S.; Das, N. S.; Sen, D.; Chattopadhyay, K. K. *J. Phys. D: Appl. Phys.* **2014**, *47*, 505301/1–9.
- (43) Einarsrud, M. A.; Grande, T. *Chem. Soc. Rev.* **2014**, *43*, 2187–2199.
- (44) Som, S.; Sharma, S. K. *J. Phys. D: Appl. Phys.* **2012**, *45*, 415102/1–11.
- (45) Wu, K.; He, H.; Lu, Y.; Huang, J.; Ye, Z. *Nanoscale* **2012**, *4*, 1701–1706.
- (46) Banerjee, A. N.; Joo, S. W.; Min, B. K. *J. Appl. Phys.* **2012**, *112*, 114329/1–8.
- (47) Mo, R.; Liu, Y. *J. Sol.–Gel Sci. Technol.* **2011**, *57*, 16–19.
- (48) Mii, O. I.; Sprague, J.; Lu, Z.; Nozik, A. J. *Appl. Phys. Lett.* **1996**, *68*, 3150–3152.
- (49) Wen, G.; Zeng, X.; Wen, X.; Liao, W. *J. Appl. Phys.* **2014**, *115*, 164303/1–8.
- (50) Ledoux, G.; Guillois, O.; Porterat, D.; Reynaud, C.; Huisken, F.; Kohn, B.; Paillard, V. *Phys. Rev. B* **2000**, *62*, 15942–15951.
- (51) Chaabouni, F.; Abaab, M.; Rezig, B. *Sens. Actuators, B* **2004**, *100*, 200–204.
- (52) Das, N. S.; Banerjee, D.; Chattopadhyay, K. K. *J. Mater. Sci.* **2013**, *48*, 750–757.
- (53) Sanchez, J. A.; Menguc, M. P. *Nanotechnology* **2008**, *19*, 075702/1–11.